Contents lists available at ScienceDirect

# Materials Science & Engineering A

# Atomistic simulation of tantalum nanoindentation: Effects of indenter diameter, penetration velocity, and interatomic potentials on defect mechanisms and evolution

C.J. Ruestes [a,b,h,*], A. Stukowski [c], Y. Tang [d], D.R. Tramontina [b], P. Erhart [e], B.A. Remington [f], H.M. Urbassek [g], M.A. Meyers [a], E.M. Bringa [b,h]

[a] Department of Mechanical and Aerospace Engineering, University of California, San Diego, La Jolla, CA 92093, USA
[b] Facultad de Ciencias Exactas y Naturales, Univ. Nac. de Cuyo, Mendoza 5500, Argentina
[c] Technische Universität Darmstadt, Darmstadt 64287, Germany
[d] Shanghai Institute of Applied Mathematics and Mechanics, Shanghai University, Shanghai 200072, China
[e] Chalmers University of Technology, Department of Applied Physics, Gothenburg 41296, Sweden
[f] Lawrence Livermore National Lab, Livermore, CA 94550, USA
[g] Physics Department and Research Center OPTIMAS, University of Kaiserslautern, Kaiserslautern 67663, Germany
[h] CONICET, Mendoza 5500, Argentina

## ARTICLE INFO

## ABSTRACT

Nanoindentation simulations are a helpful complement to experiments. There is a dearth of nanoindentation simulations for bcc metals, partly due to the lack of computationally efficient and reliable interatomic potentials at large strains. We carry out indentation simulations for bcc tantalum using three different interatomic potentials and present the defect mechanisms responsible for the creation and expansion of the plastic deformation zone: twins are initially formed, giving rise to shear loop expansion and the formation of sequential prismatic loops. The calculated elastic constants as function of pressure as well as stacking fault energy surfaces explain the significant differences found in the defect structures generated for the three potentials investigated in this study. The simulations enable the quantification of total dislocation length and twinning fraction. The indenter velocity is varied and, as expected, the penetration depth for the first pop-in (defect emission) event shows a strain rate sensitivity $m$ in the range of 0.037–0.055. The effect of indenter diameter on the first pop-in is discussed. A new intrinsic length-scale model is presented based on the profile of the residual indentation and geometrically necessary dislocation theory.

© 2014 Elsevier B.V. All rights reserved.

## 1. Introduction

Nanoindentation is an experimental technique of ever increasing importance, both in research and technology. It is not only used to gather information about the elastic modulus and hardness of a material [1,2] but also provides insights into cracking mechanisms [3], fracture toughness [4], strain-hardening [5], phase transformations [6], creep [7], and the mechanical response of superhard thin films [8]. The technique is particularly useful but not limited to thin films and surface layers. The combination of the modern experimental testing method with the Oliver–Pharr [9] analysis has led to a widespread utilization of nanoindentation testing.

Since the seminal contribution by Kelchner et al. [10], molecular dynamics (MD) simulations have been extensively applied to study plasticity mechanisms during indentation processes, mainly on fcc (face centered cubic) metals [11–22]. Contributions to the study in bcc (body centered cubic) metals are, however, rare [23–25], primarily because of the scarcity, up to recently, of robust potentials. Hagelaar et al. [25] investigated the nanoindentation of tungsten using a Finnis-Sinclair (FS) potential, focusing on small penetration depths. Naveen et al. [23] studied dislocation activation from different slip systems in Fe and Fe–Cr, using a composition-dependent embedded atom model (CDEAM) potential by Caro et al. [26]. Alcalá et al. [24] recently studied Ta using the Embedded Atom Method (EAM) potential by Li et al. [27], reporting nucleation of planar defects, including stacking faults and twins. Empirical potential development is complex [28], and part of the reason for the relative scarcity of nanoindentation simulation results on bcc metals is the lack of potentials which are both computationally efficient and reliable at high strains [29]. Nanoindentation simulations in particular might

* Corresponding author at: Facultad de Ciencias Exactas y Naturales, Universidad Nacional de Cuyo, Mendoza M5502JMA, Argentina. Tel.: +54 261 4236003; fax: +54 261 4236003.
E-mail address: cjruestes@hotmail.com (C.J. Ruestes).

often reach and exceed the application limits for which a given potential was intended and tested.

The plastic stages after the pop-in event during nanoindentation are still a fertile area for both simulation and experimental studies [18] and the general purposes of this work are (a) to study the initiation and evolution of defects at the onset of plasticity in a bcc metal using nanoindentation as the deformation tool, and (b) to compare several different empirical potentials. The material selected for this study is bcc tantalum. Extensively studied experimentally, its high melting point and bcc phase stability up to pressures well above 100 GPa, make it a model material for studying bcc plasticity [30–32].

We first present the elastic constants as a function of pressure calculated by each potential, followed by the typical surface energies. Then we focus on the onset of plasticity and analyze its evolution by quantifying dislocation density and twinning and identifying the dislocation evolution mechanisms, we discuss tip diameter and indenter velocity effects on the elastic portion and onset of plasticity, and present the residual micro-structures for each potential. Finally, we present a new intrinsic length-scale model based on the profile of the residual indentation, using the concept of geometrically necessary dislocations.

## 2. Methods

### 2.1. Simulation

Molecular dynamics simulations were carried out with LAMMPS [33], including defect nucleation and load–penetration curves to study the influence of the interatomic potential on the results and to address potential-dependent behaviour [28]. Three interatomic potentials were used and the predictions compared: the Embedded Atom Method (EAM) potential by Li et al. [27], the Extended Finnis-Sinclair (EFS) potential by Dai et al. [34], and the recent EAM potential by Ravelo et al. [30,31]. These will be referred, for the sake of simplicity, as Li-EAM, Dai-EFS, and Ravelo-EAM potentials.

We used a rigid hemispherical indenter interacting with the atoms in the target with a harmonic potential, $Vi = K(R - r_i)^2$, with $R$ the indenter radius and $r_i$ the position of atom $i$, and with $K = 1000$ eV/nm$^2$ being the specified force constant. Even though the pyramidal Berkovich indenter is the most common indenter used in nanoindentation because it maintains self similarity, such an indenter has a rounded tip with a radius of up to 150 nm. Cube corner nanoindentation tips can have a radius as small as 40 nm. Therefore, it can be expected that the spherical tip used in our studies renders the same plasticity mechanisms produced by a Berkovich tip or a cube corner tip prior to significant effects produced by the pyramidal planes. A Langevin bath at 300 K was applied to the sides and bottom of the simulation domain in order to minimize possible boundary effects. For each configuration, the entire sample was energetically minimized and equilibrated at 300 K prior to nanoindentation. We restricted our simulations to the three principal surface orientations: (100), (110) and (111) single crystals.

The simulations were carried out with indenter tip diameters (D) of 8, 12, 16 and 20 nm, the latter for the (100) oriented surface only. The simulation box was varied according to indenter size: $24 \times 24 \times 12$ nm$^3$ ($\sim 0.4$ million atoms), $36 \times 36 \times 18$ nm$^3$ ($\sim 1.3$ million atoms), $48 \times 48 \times 24$ nm$^3$ ($\sim 3$ million atoms), and $60 \times 60 \times 30$ nm$^3$ ($\sim 6$ million atoms), respectively. In each case, the box size was much larger than the expected extent of the plasticity zone, which is estimated to be up to 3.5 times the radius of the indentation imprint, as a worst-case scenario [35,36]. Our box sides were chosen to be around 6 times the radius of the imprint in the Z direction and 8 times the radius of the imprint in

the X and Y directions. In addition we have ensured that using a much larger box (20 million atoms) for the 20 nm indenter did not change the resulting micro-structure.

MD simulations were conducted in a displacement-controlled fashion by applying a constant penetration rate to the indenter [10,24]. For our simulations, a constant penetration rate of 34 m/s was chosen, and we established the effect of the imposed strain rate by comparing results from 34 and 3.4 m/s loading velocity. We note that these indentation speeds correspond to $\sim 1/100$ $C_0$ and $\sim 1/1000$ $C_0$ respectively, where $C_0$ is the directionally averaged sound velocity for Ta.

In every case, after achieving a penetration of 30% of the indenter diameter, the indenter was held in position for a time equal to one-tenth of the loading time, and then removed at the same displacement rate until no load was measured. Hold periods are a common practice in experimental nanoindentation, for example, in thermal drift and creep measurements [1], and we intended to observe some level of plastic relaxation during the hold, which indeed occurred.

Defective structures were filtered by Common Neighbor Analysis (CNA) [37] and by means of the recently developed Dislocation Extraction Algorithm [38–40], and visualized using OVITO [41].

## 3. Evaluation of interatomic potentials

### 3.1. Purpose of the evaluation

There is no source in the literature of interatomic potentials specifically fitted for nanoindentation studies. When studying bcc metals, potentials of the Embedded Atom Method style [42] and of the Extended Finnis-Sinclair style [34] are used extensively, among others, due to a relatively good balance between accuracy and computational cost. Even when choosing a widely used potential, the elected one should confirm not only its stability and surface energies but also the absence of unphysical behavior such as non-valid slip systems or solid–solid phase transitions not predicted by a phase diagram [28]. The Li-EAM potential was recently used in nanoindentation simulations [24] and high strain-rate simulations of deformation and fracture in nano-crystalline tantalum thin films [43] but is not fitted to high strains/high pressure. The Dai-EFS and, in particular, the Ravelo-EAM potentials were both fit to high pressure properties. Both of them have been extensively used in high-pressure/high strain-rate simulations [30,31]. Thus, a comparison of the three potentials is warranted. The following sections are devoted to the evaluation of the three potentials chosen in the present study.

### 3.2. Elastic properties

The elastic behavior of structures with cubic symmetry is described completely by their elastic constants, $C_{11}$, $C_{12}$, and $C_{44}$. The elastic constants obtained using the three potentials were calculated. Elasticity equations were used to convert them into the standard.

The orientation-dependent elastic modulus for (100), (110), and (111) single crystals were calculated by means of the following equations [44]:

$$\frac{1}{E_{100}} = \frac{C_{11} + C_{12}}{(C_{11} + 2C_{12})(C_{11} - C_{12})}. \tag{1}$$

$$\frac{1}{E_{110}} = \frac{4C_{44}(C_{11} + C_{12}) - 2C_{44}(C_{11} + 2C_{12}) + (C_{11} + 2C_{12})(C_{11} - C_{12})}{4C_{44}(C_{11} + 2C_{12})(C_{11} - C_{12})}. \tag{2}$$

$$\frac{1}{E_{111}} = \frac{6C_{44}(C_{11}+C_{12}) - 4C_{44}(C_{11}+2C_{12}) + (C_{11}+2C_{12})(C_{11}-C_{12})}{6C_{44}(C_{11}+2C_{12})(C_{11}-C_{12})}. \tag{3}$$

$B$ is the bulk modulus, defined as

$$B = \frac{C_{11}+2C_{12}}{3}. \tag{4}$$

The shear modulus $G$ was defined as the arithmetic mean over the Voigt-averaged and Reuss-averaged shear moduli

$$G = \frac{1}{2}(G_{Voigt} + G_{Reuss}). \tag{5}$$

According to Ziegenhain et al. [17], $G_{Reuss}$ [45] is defined as

$$G_{Reuss} = \frac{5(C_{11}-C_{12})C_{44}}{4C_{44} + 3(C_{11}-C_{12})}. \tag{6}$$

$G_{Voigt}$, the Voigt-averaged shear modulus [46], is defined as

$$G_{Voigt} = \frac{C_{11}-C_{12}+3C_{44}}{5}. \tag{7}$$

$\nu$ is the Poisson ratio, defined as

$$\nu = \frac{3B-2G}{2(G+3B)}. \tag{8}$$

The Elastic modulus, $E$, is

$$E = 2G(\nu+1) \tag{9}$$

The elastic anisotropy can be described by the Zener anisotropy factor, $X$, as

$$X = \frac{2C_{44}}{C_{11}-C_{12}}. \tag{10}$$

Predictions from Eqs. (1)–(10) are summarized in Table 1. Potentials reproduce reasonably well the elastic properties at zero pressure.

Nanoindentation typically leads to large stresses up to tens of GPa and it is important to establish whether the pressure dependence of the elastic constants is adequate; this is shown in Fig. 1. The Dai-EFS and Ravelo-EAM potentials behave well under pressure and in the range considered here, while it can be seen that the Li-EAM potential performs poorly at pressures which can be

**Table 1**
Elastic properties of Ta at zero pressure by the potentials of Li et al. [27], Dai et al. [34] and Ravelo et al. [31], together with experimental values by Stewart et al. [47]. Elastic constants $C_{ij}$, bulk modulus $B$, average shear modulus $G$, average Poisson ratio $\nu$, elastic anisotropy $X$, average elastic modulus $E$, and elastic modulus for the three crystallographic orientations studied.

| | $C_{11}$ (GPa) | $C_{12}$ (GPa) | $C_{44}$ (GPa) | G (GPa) | $\nu$ (GPa) | X | E | $E_{100}$ (GPa) | $E_{110}$ (GPa) | $E_{111}$ (GPa) |
|---|---|---|---|---|---|---|---|---|---|---|
| Li-EAM | 263 | 159.1 | 86.5 | 68.1 | 0.343 | 1.66 | 183 | 140 | 197 | 400 |
| Dai-EFS | 230.8 | 143.5 | 91.3 | 67.9 | 0.325 | 2.09 | 180 | 120 | 189 | 405 |
| Rav-EAM | 262.6 | 160.7 | 81.8 | 67.2 | 0.345 | 1.6 | 181 | 140 | 190 | 385 |
| Exp. | 264 | 160 | 82 | – | – | – | – | – | – | – |
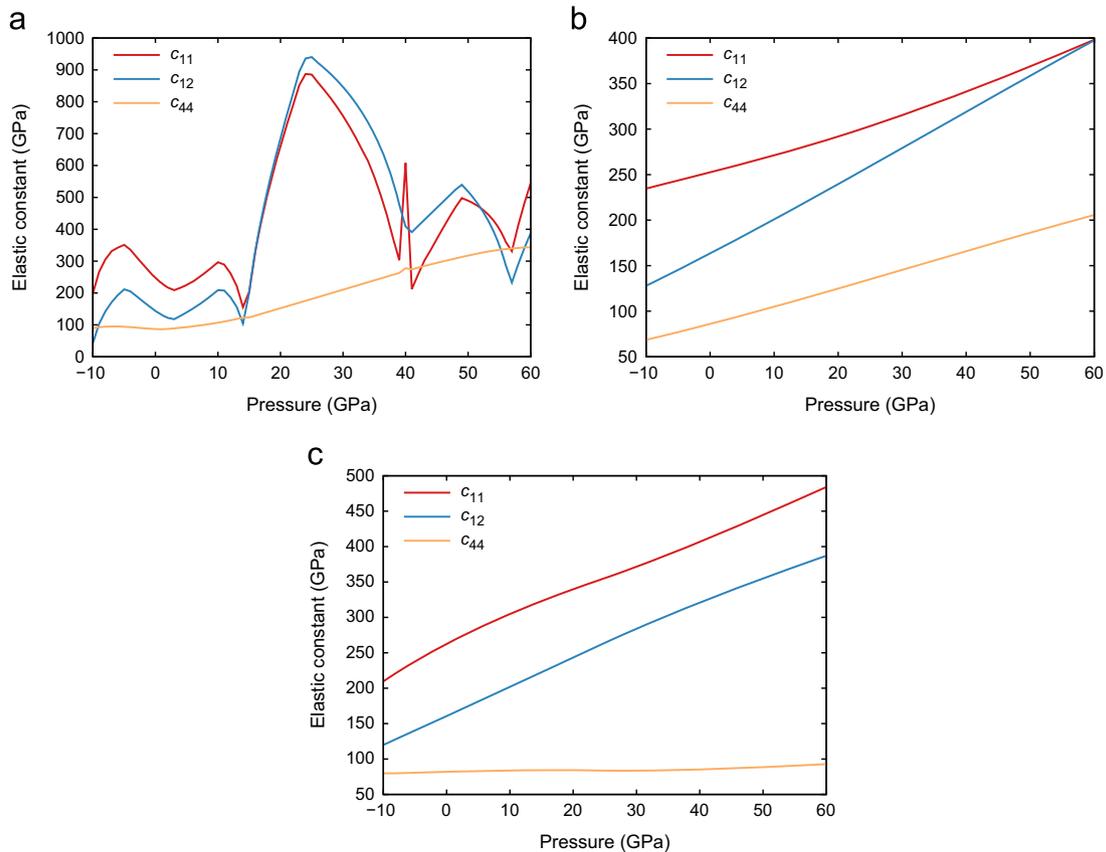


**Fig. 1.** Pressure dependence of the elastic constants $C_{ij}$ for the potentials studied: (a) Li-EAM, (b) Dai-EFS, and (c) Ravelo EAM.

reached during nanoindentation. As shown in Fig. 1, the elastic constants for the Li potential also display discontinuities under compression. This is possibly due to the spline fitting used for this potential, which was not tested at large strains. The discontinuities in the derivative of the elastic constants can lead to artificial effects during loading, such as artificial micro-structures and phase transitions [32] as well as soft phonon modes [48].

### 3.3. Generalized stacking fault energies

In fcc metals plasticity often occurs by emission of partial loops, i.e. partial dislocations bounding a stacking fault. In bcc metals, in contrast, the generalized stacking fault energy, also known as the $\gamma$ energy surface, does not exhibit local minima for the relevant $\langle 111 \rangle$ shear directions [49], and stacking fault formation is not expected. However, Tang et al. [50] and Alcalá et al. [24] describe stacking faults for the Dai-EFS and Li-EAM potentials, respectively. Therefore, generalized stacking fault energy (GSFE) surface calculations for Ta along the $\langle 111 \rangle$ slip directions were performed for the three potentials used in this study, and are shown in Fig. 2.

The Dai-EFS potential gives the lowest stacking fault energy, and displays asymmetry for the {112} plane, as in recent Density Functional Theory (DFT) calculations [51]. Curves using the Ravelo-EAM potential are symmetric for both planes, as in other DFT calculations [52]. The curves for Li-EAM are not smooth, probably due to the splines chosen for potential fitting which also caused the discontinuities in the elastic constants.

The presence of stacking faults can dramatically alter the evolution of deformation, as is well known experimentally and has been shown computationally. For instance, the defect configuration generated around an expanding void is quite different in copper [53] than in tantalum [50] (no stacking fault formation).

In all potentials used here the {110} plane along $\langle 1\bar{1}1 \rangle$ shear direction always has the lowest energy and, therefore, unstable stacking faults (SFs), if exist, might preferentially form on these planes. These SFs would be purely 'elastic', and correspond to the incipient stage of 'plastic' defects that will form later on. Tang et al. [50] observed that the nucleation of dislocations in [110] can occur by formation of two SFs, when studying the defect nucleation and evolution under uniaxial high strain rate compression of a nano-void in a Ta single crystal. Small segments of {110} SFs were seen using the Dai-EFS potential. The fault vector is actually $1/6\langle 1\bar{1}0 \rangle$ and could be considered as a combination of two vectors $1/12\langle 1\bar{1}1 \rangle + 1/12\langle 1\bar{1}\bar{1} \rangle$. The SFs observed by Alcalá et al. [24] with the Li-EAM potential, with a reported fault vector of $1/2\langle 1\bar{1}0 \rangle$, could be the same as the ones observed by Tang et al. [50] when using the Dai-EFS potential. The reported value of $1/2\langle 1\bar{1}0 \rangle$ seems unlikely, since its magnitude is too large, close to the Burgers vector of a full dislocation $1/2\langle 111 \rangle$. The fault vector of a {112} twin is only $1/6\langle 111 \rangle$. So the $1/6\langle 1\bar{1}0 \rangle$ value reported by Tang [50] is a more reasonable value. Nevertheless, these SFs are unstable and they either transform to other stable defects or recover completely during unloading, while full dislocations and twins can survive. Pressure might modify the GSFE surface [54], and further studies are needed to quantify possible pressure-induced changes.

The role of generalized twinning fault energy (GTFE) surface in plasticity of bcc nanowires was discussed by Cao [55]. In this work, the following definitions were used: the twinning fault (TF) is the energy measured at a displacement $b/3$, unstable and stable twinning fault (UTF and STF, respectively) energies are the energy maximum and minimum along the GTFE curve, the twin migration (TM) energy is the difference between UTF and TF energies, $(UTF - TF)$, and the twin propensity is given by the ratio $UTF/USF$. Since the UTF exists only in fcc, the STF is used in bcc metals instead. A twin propensity ratio below 1 usually indicates
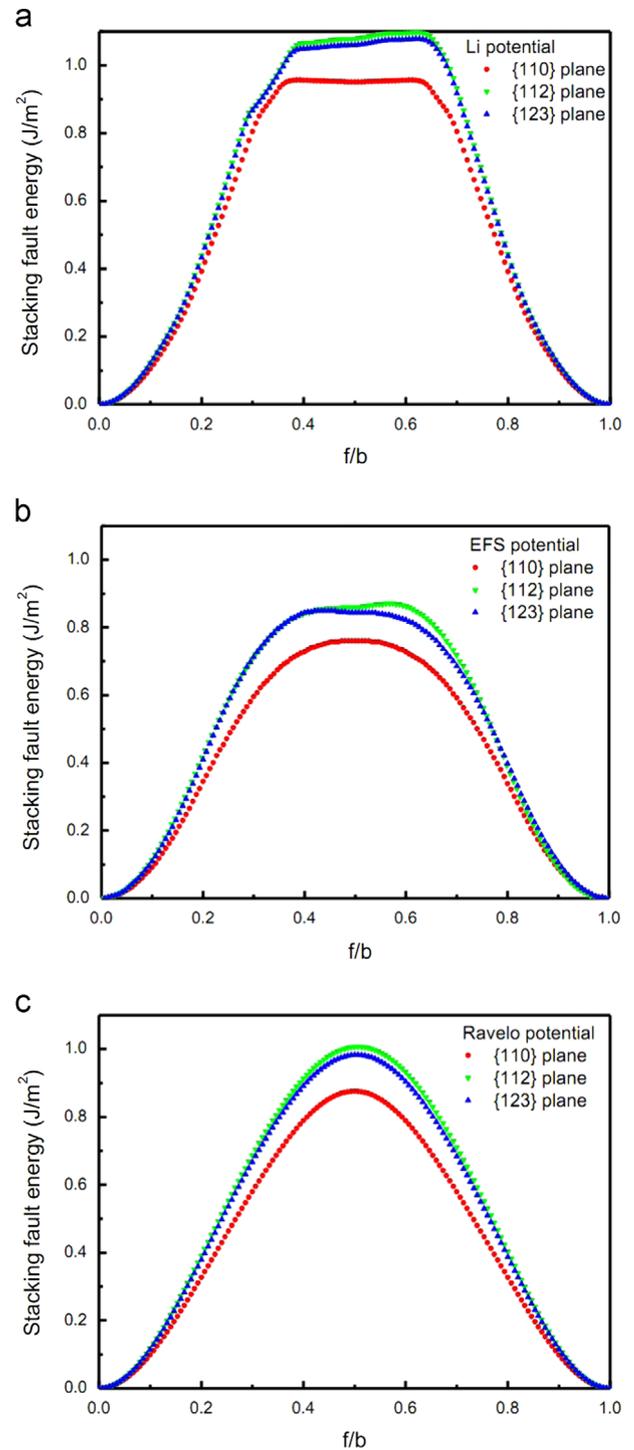


Fig. 2. Comparison of stacking fault energies for Ta using the three potentials: (a) Li-EAM, (b) Dai-EFS, and (c) Ravelo EAM. The {110} plane always has the lowest energy. The Dai-EFS potential captures the twinning-antitwinning asymmetry for {112} plane found by DFT calculations [51].

that twinning is dominant over subsequent slip. We show the GTFE curve for the three potentials studied here, calculated as in [55] at zero pressure in Fig. 3. For all potentials, $STF/USF < 1$, $STF/TF < 1$, $TM < 0$, and $|TM/USF| \ll 1$. Therefore, twinning should be preferred over slip and twins would grow thanks to a low migration barrier. Li-EAM has the largest STF-TF difference, suggesting the largest driving force for twinning. However, as for the GSFE surface, finite pressure might significantly change the GTFE surface.
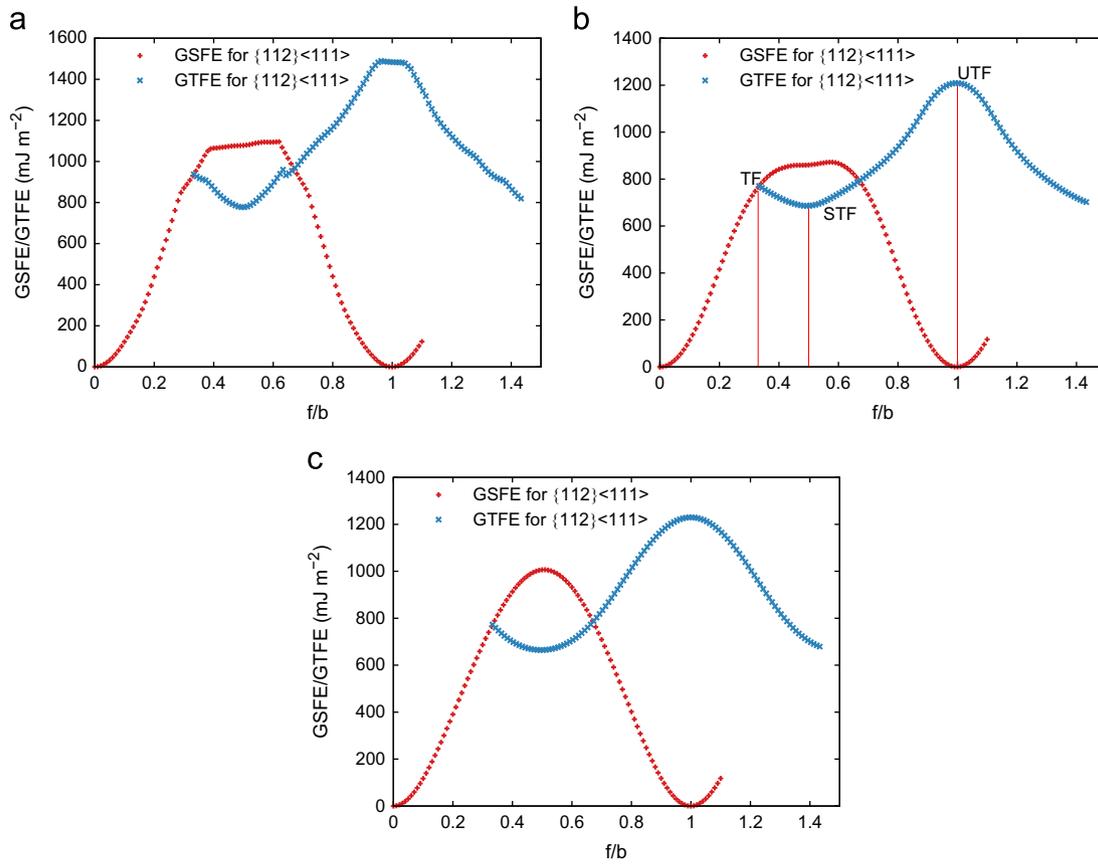
**Fig. 3.** Generalized twinning fault energy curve for the three potentials compared with generalized stacking fault energy for {112} ⟨111⟩. (a) Li-EAM, (b) Dai-EFS and (c) Ravelo-EAM.

As a direct consequence of the behavior of the Li-EAM potential shown in Figs. 1a, 2 and 3a, it was tested on (100) single crystals only, to demonstrate unexpected response as presented in the next sections.

## 4. Nanoindentation simulation results

### 4.1. Classical treatment of nanoindentation loading

In his seminal contribution, Hertz studied the elastic interaction between a sphere of radius $R$ and an elastic isotropic solid [56]. He determined that the force $F$ imparted by the sphere perpendicular to the surface is related to the displacement $h$ into the surface through the following relationship:

$$F = \frac{4}{3} E^* R^{1/2} h^{3/2}. \tag{11}$$

$E^*$ is often called the "reduced indentation modulus" or "combined indentation modulus" of the system, and is given by

$$\frac{1}{E^*} = \frac{1-\nu^2}{E} + \frac{1-\nu'^2}{E'}, \tag{12}$$

where $E$, $\nu$, $E'$ and $\nu'$ are the elastic modulus and Poisson's ratio of the surface and indenter, respectively. The indenter used in our simulations [10] is assumed to be rigid and, hence, the second term in Eq. (12) is dropped. Also, our indenter is frictionless, analogous to a Hertzian indenter and, therefore, there are no forces in the direction tangential to the tip. Within the Hertzian

model, the contact pressure amounts to

$$p = \frac{3}{4\pi} \frac{1}{E^*} \sqrt{\frac{h}{R}}. \tag{13}$$

The Hertz treatment is considered exact for $h \ll R$ and an elastically isotropic solid. It has been shown [57,58,17] that when treating single crystals, as in our study, the Hertzian laws hold with a modified indentation modulus that depends on the surface orientation. Hence for our single crystals,

$$\frac{1}{E^*} = \frac{1-(\nu_{ijk})^2}{E_{ijk}}. \tag{14}$$

The above equations will be used to calculate Hertzian loading curves and compare them to the MD loading curves.

### 4.2. The onset of plasticity

For our simulations, the relevant geometrical parameters can be schematically seen in Fig. 4a, together with an arrangement of geometrically necessary dislocations [59] under the indentation (Fig. 4c and d). A typical force–displacement curve for a nanoindentation test can be seen in Fig. 4b. A spherical indenter is pressed into the sample at constant penetration rate and the equivalent reaction force $F$ is computed based on the interactions tracked by the MD code. We are able to measure the contact radius $a_p$ and the penetration depth, both relative to the surface ($h$) and relative to the contact circle ($h_p$), see Fig. 4a. The hardness, $H$, is given by

$$H = \frac{F_{max}}{A}, \tag{15}$$
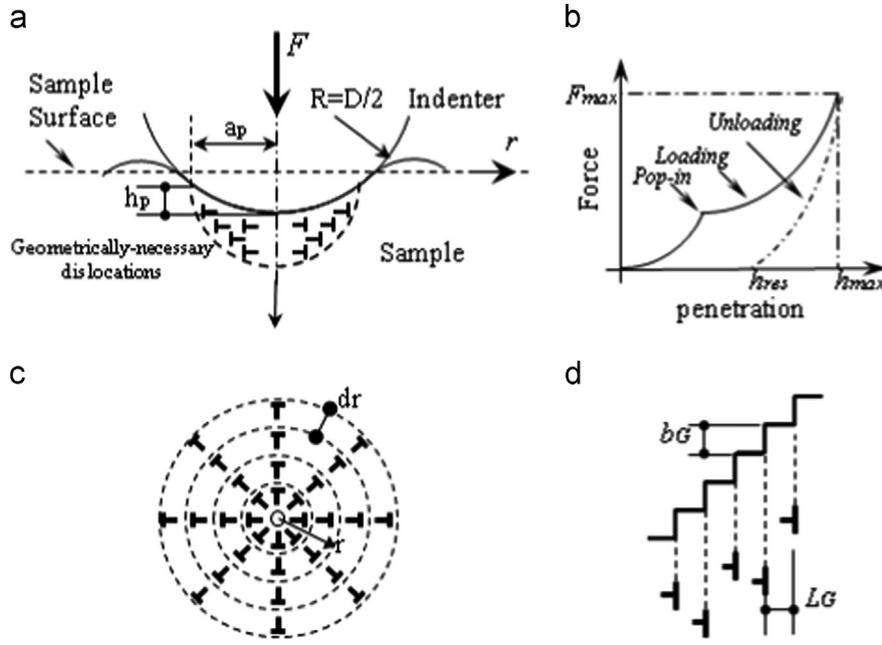
**Fig. 4.** (a) Specimen is indented by a rigid spherical indenter. (b) Typical load–displacement curve showing the loading (indenter penetration) stage and the unloading (indenter removal) stage. (c and d) Geometrically necessary dislocations created during the process. Dislocation structure is assumed to be circular dislocation loops. Figure inspired by Refs. [60–62].

where $F_{max}$ is the load and $A$ is usually taken as the projected area of the residual impression. In nanoindentation testing, the size of the residual impression can be very complex and of questionable accuracy [17], so the residual depth, $h_{res}$, is measured instead, and the contact area is assumed to be [1]:

$$A \approx 2\pi R h_{res}. \qquad (16)$$

In some load-controlled nanoindentation experiments, the irreversible onset of plastic deformation can be seen in the force–displacement curve as an excursion in depth at constant load. This event is often referred to as a "pop-in" [63] and, for defect-free crystals, is linked particularly to dislocation nucleation at or just below the surface [64–66]. In our simulations, the indentation is performed at constant penetration rate, and pop-in events can appear either as a load drop for a low penetration rate or as an excursion in depth for sufficiently high penetration rates [24].

Load–penetration curves for the three potentials using a spherical tip diameter of 20 nm are presented in Fig. 5. The Hertz equation describes the elastic loading curve very well up to the onset of plasticity. Hardness measurements for our simulations, using Eqs. (15) and (16), are presented in Table 2. Typically, hardness decreases with indenter diameter, and reaches a value around 14–18 GPa, which is higher than experimental values [65,67], consistent with typical high values for MD simulations of perfect crystals.

Continuing with a classical treatment, the contact radius $a_p$ was established at the onset of plasticity, and the mean contact pressure was calculated through

$$p_{mean} = \frac{F}{\pi a_p^2}. \qquad (17)$$

The maximum resolved shear stress is related to the mean contact pressure and reaches a maximum of $\tau_{max} \sim 0.465 p_{mean}$ slightly below the contact surface [64]. Our calculations for the 20 nm tip diameter give $\tau_{max} \sim 13.2$ GPa for Li-EAM, $\tau_{max} \sim 14.4$ GPa for Dai-EFS, and $\tau_{max} \sim 9.7$ GPa for Ravelo-EAM. These values are derived only based on the corresponding elastic constants, and the two former values are above the theoretical
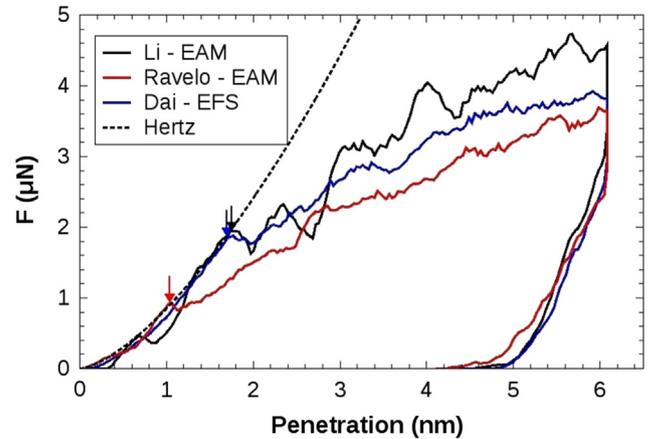


**Fig. 5.** Comparison of load – hold – unload indentation curve for the three potentials employed together with a Hertzian solution for an indenter diameter of 20 nm. Experimental elastic constants were used for the Hertzian solution. Arrows indicate the end of the elastic regime, followed by the elasto-plastic transition. Once the maximum prescribed depth is reached, the indenter was held in position, which translates into a vertical line as the complex stress field gets relaxed and the load measured at the indenter decreases. After the holding stage, the unloading was performed by removing the indenter at a constant rate, until full unload is reached (zero force at the indenter).

**Table 2**
Hardness measurements (GPa) on Ta (100), for all indenter diameters $D$ (nm), for the different potentials studied.

| $D$ (nm) | Li-EAM (GPa) | Dai-EFS (GPa) | Ravelo-EAM (GPa) |
|---|---|---|---|
| 8 | 21 | 19.9 | 15.7 |
| 12 | 17.7 | 17.7 | 14.9 |
| 16 | 17.6 | 16.3 | 14.3 |
| 20 | 16.6 | 16.6 | 14.0 |

threshold for homogeneous nucleation ($\tau_{th} = G/2\pi$), while the latter is slightly below this threshold, possibly due to the different behaviour of the elastic constants under pressure. It should be noticed that the Orowan value ($G/2\pi$) is only a first-order estimate

of the theoretical strength, and that more exact calculations predict values that are significantly different. A threshold above the ideal value for homogeneous nucleation is not unexpected, because of a possible pressure hardening effect [66]. The occurrence of pressure hardening in Ta has been reported by Park et al. [68] and is attributed to the pressure dependence of the shear modulus, which increases with pressure, hence increasing the threshold. The pressure hardening effect during nanoindentation has also been verified before [17]. Schuh et al. [69] demonstrated that the first pop-in event requires a large critical stress. Both Dai-EFS and Ravelo-EAM display similar pressure hardening but quite different thresholds, pointing to the complexity of dislocation nucleation. For instance, Ogata [66] pointed out that nucleation might be driven by stress gradients, not stress maxima. Recently, Kang et al. [70] reported a complex behavior of the shear stress needed to move a dislocation, depending on the exact angle of the applied shear, with mobility showing a faceted behavior.

It is customary in experiments to indicate pop-in events in terms of the dimensionless ratio $a_p/D$, where $D$ is the tip diameter. For {001} Ta surface, experiments and previous simulations indicate that $a_p/D \sim 0.19 \pm 0.01$ at 293 K [24]. Our results show $a_p/D^{Li} = 0.21 \pm 0.02$, $a_p/D^{EFS} = 0.21 \pm 0.01$, $a_p/D^{Rav} = 0.17 \pm 0.01$ for the 20 nm diameter tip indenter.

Hardness measurements for our simulations, using Eqs. (15) and (16) are presented in Table 2 for (100) single crystals and in Table 3 for (110) and (111) single crystals. There is a decrease in hardness with the potential and diameter of the indenter $D$, with $H_{Li-EAM}$ being the highest and $H_{Ravelo-EAM}$ the lowest. The effect of the indenter diameter is similar to the indentation size effect reported by Swadener [71], that is hardness decreases as indenter diameter increases, without the influence on the penetration depth or contact radius. The hardness in the (111) single crystal is the lowest, and this is probably due to the greater availability of shear directions.

**Table 3**
Hardness measurements (GPa) on Ta (110) and (111).

| $D$ (nm) | Ta (110) Dai-EFS (GPa) | Ta (110) Ravelo-EAM (GPa) | Ta (111) Dai-EFS (GPa) | Ta (111) Ravelo-EAM (GPa) |
|---|---|---|---|---|
| 8 | 19.5 | 19.2 | 14.8 | 14.7 |
| 12 | 19.3 | 18.8 | 14.2 | 14.1 |
| 16 | 18.2 | 17.6 | 13.9 | 13.9 |

### 4.3. Indentation rate effects on elastic deformation and the onset of plasticity

Additional simulations were performed at a penetration velocity of 3.4 m/s ($\sim 1/1000\,C_0$) to establish the effect of strain rate on the indentation of (001) Ta using the 20 nm diameter tip. The results are plotted in Fig. 6. As expected, the critical load to induce plasticity depends on the penetration velocity. The critical load is lowered by 9% for Dai-EFS, and 11% for Ravelo-EAM for a ten fold decrease in penetration velocity (and associated strain rate). One can extract an exponent for the strain rate sensitivity using the stress at which plastic deformation is first noticeable (pop-in stress) divided by the ratio of strain rates, which we assume to be equal to the ratio of velocities:

$$m = \frac{\log \sigma_1/\sigma_2}{\log \dot{\epsilon}_1/\dot{\epsilon}_1} = \frac{\log \sigma_1/\sigma_2}{1} \qquad (18)$$

The corresponding values are, for the two potentials: Dai-EFS: $m=0.037$; Ravelo-EAM: $m=0.055$. These values are in line with the known strain rate sensitivity of Ta in the thermally activated regime since values reported in the literature are in this range: Rajendran et al. [72]: $m \sim 0.04$–0.1; Hoge and Mukherjee [73]: $m=0.075$. However, the strain-rates are on the order of $10^8$–$10^9\,s^{-1}$ and this regime is definitely not in the realm of thermal activation.

In every case, the onset of plasticity occurs due to homogeneous nucleation of planar defects, as recently reported by Alcalá et al. [24], and in agreement with the onset of plasticity from a void, which has a similar geometry, reported earlier by Tang et al. [50,74].

### 4.4. Tip diameter effect on elastic curve and onset of plasticity

For all diameters studied here (8–20 nm), the onset of plasticity occurs by the nucleation of planar defects, as discussed before. A few ps after the onset of plasticity, twins appear for every potential and every tip diameter used in our MD simulations. Then, dislocation shear loops nucleate, with cross-slipping of screw segments as the indentation proceeds, leading to prismatic loop emission for the Dai-EFS and Ravelo-EAM potentials. The Li-EAM potential does not reveal prismatic loop emission for an indentation speed of 34 m/s, at any tip diameter. It does emit prismatic loops for 3.4 m/s and 20 nm diameter tip, which is evidence for a strong velocity dependence. Hagelaar et al. [25] showed prismatic loop emission for a 10 nm diameter indenter
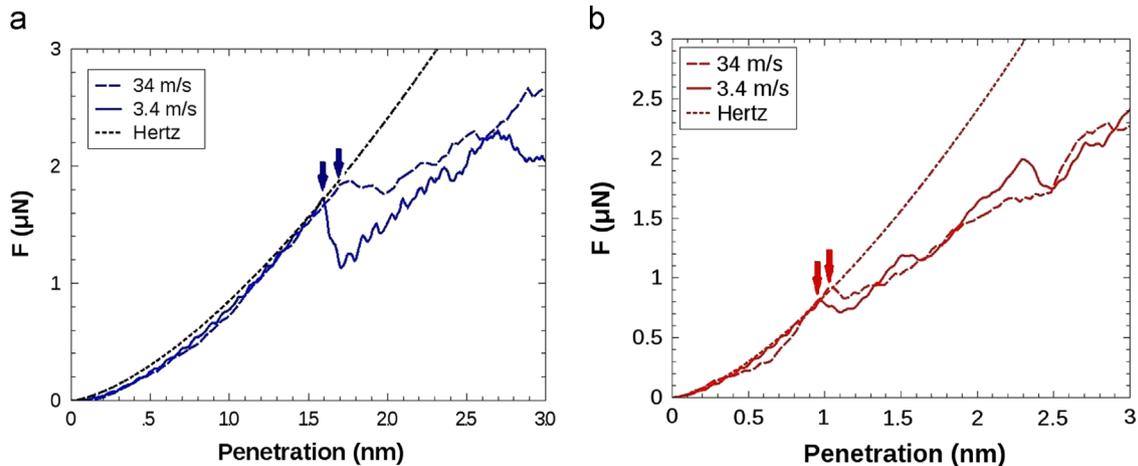


**Fig. 6.** Indenter velocity dependence of the loading curves for the three potentials and a 20 nm diameter tip. The Hertz approximation was calculated with the elastic constants for each potential. Arrows indicate the onset of plasticity. As the penetration rate decreases, the first pop-in event becomes more noticeable, with a marked reduction in load at the onset of plasticity. (a) Dai-EFS and (b) Ravelo-EAM.

from a W (111) surface, but their mechanism seems to be direct loop punching and not the dislocation reactions observed in our case.

Figs. 7 and 8 reveal that both the point at which the onset of plasticity occurs and the slope of the elastic-plastic stage increase with increasing diameter.
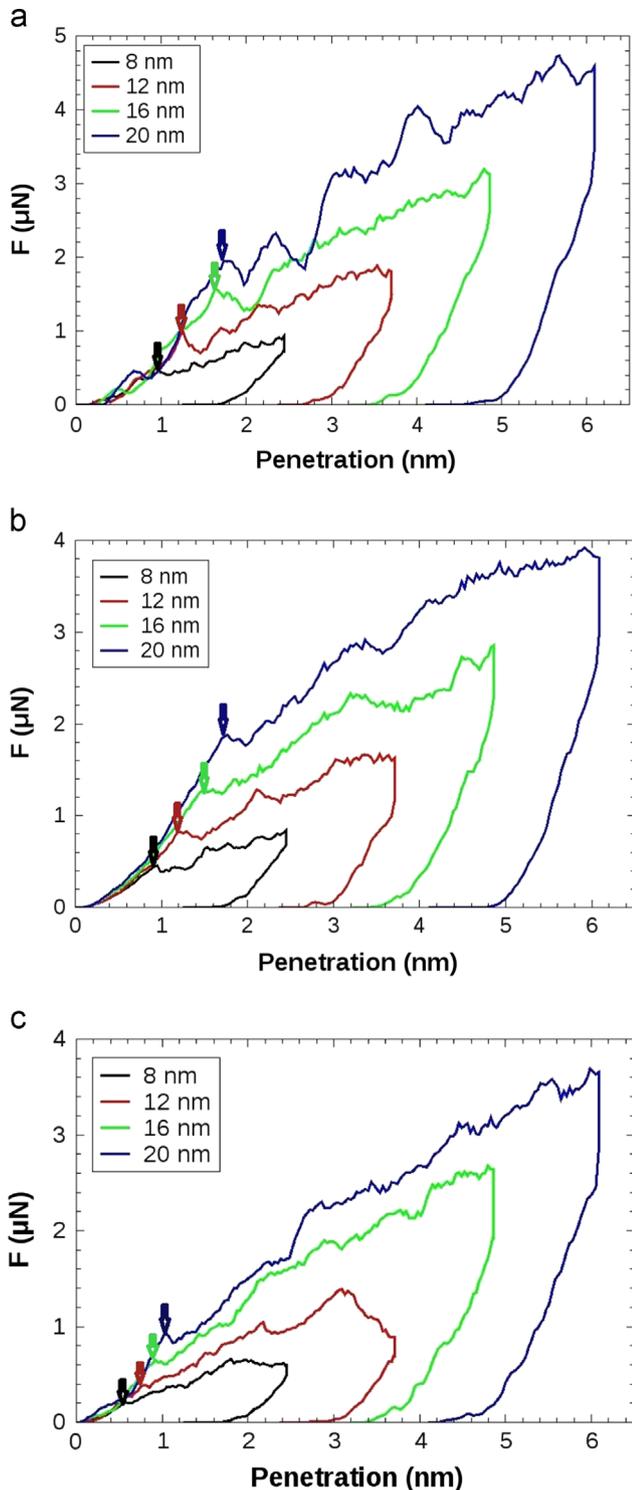


**Fig. 7.** Ta (100): on indenter size dependence of the loading curves for the three potentials. 8, 12, 16 and 20 nm denote the diameter of the spherical tip used for the simulation. Note the jagged behaviour for Li and Ravelo EAMs in the elastic loading portion. After the onset of plasticity, indicated with arrows, no significant difference is found in the slope of the elasto-plastic regime amongst different indenter sizes for each potential. (a) Li-EAM, (b) Dai-EFS and (c) Ravelo-EAM.

## 4.5. Plasticity mechanisms during loading

Past the initial defect-nucleation stage, plasticity evolves as a balance of two well-known and distinctive mechanisms: twinning and dislocation activity. This is shown below for the indentation along [100].

The Li-EAM potential produces profuse twinning starting in the early stages of plasticity. As the indenter continues penetrating, the interaction of twins produces a nest-like arrangement of twins, as it can be seen in Fig. 9. This structure acts as a stable set of planar defects from which dislocation loops evolve. The twin volume fraction is 0.8% at the end of the loading stage. This structure is penetration-rate dependent, since it appears only for an indentation speed of 34 m/s, but not for 3.4 m/s. It is this unexpected behavior together with the results shown in Figs. 1a, 2 and 3a, that lead us to discard the use of this potential for the rest of the study.

The Dai-EFS potential also produces stable twins (Fig. 10a), with a volume fraction of 0.3%, but with typical twin lamellae being formed near the surface. The Ravelo-EAM potential also produces twinning (Fig. 10c), achieving a volume fraction at the end of the loading stage of 0.25%, matching the Dai-EFS values closely, except at the end of unloading, where all twins disappear.

Large twin volume fractions in Ta deformed at high strain rates were previously reported using both the EFS [75] and Ravelo potentials [32]. It must be pointed out that twinning often appears under high strain rate conditions, and the twinning observed in our simulations might not appear for indentation velocities approaching experimental values, which are outside the reach of current large scale atomistic simulations. However, experiments on nanoindentation of nanocrystalline Ta (grain sizes 10–30 nm) [76], where twinning might be easier due to the nanoscale grain sizes, show that deformation proceeds by means of twinning. To the best of our knowledge, there are no nanoindentation experiments for Ta single crystals showing twinning. The small twin fractions we observe in our simulations would be difficult to detect experimentally, even with High Resolution Transmission Electron Microscopy (HRTEM).

Dislocation activity during indentation also differs for each potential, as shown in Fig. 10. There are several aspects, some of them potential dependent, that are revealed by the computations. A process of twin annihilation [24] occurs for all potentials, leading to the generation of dislocation loops.

For the Dai-EFS and Ravelo-EAM potentials, dislocation loops evolve in {110}, {112} and {123} planes with ⟨111⟩ directions, consistent with the three bcc slip systems. The screw segments of the dislocation loops cross-slip, leading to the generation of prismatic loops, which further move along ⟨111⟩ directions. The resulting structures at the end of the loading stage are presented in Fig. 10. Prismatic loop formation is more profuse for the Ravelo-EAM potential (Fig. 10). Dislocation structures for the Dai-EFS and Ravelo-EAM potentials are qualitatively similar at 34 m/s and 3.4 m/s.

Dislocation generation and multiplication can be quantified by computing the total dislocation length (Dislocation Extraction Algorithm – DXA) which can then be compared to the geometrically necessary dislocations length and the statistically stored dislocations length. Geometrically necessary dislocations are those related to strain gradients, such as the ones commonly produced by nanoindentation, while statistically stored dislocations account for species which do not produce strain gradients, such as prismatic loops and dislocation dipoles [77,78].

Following Hua and Hartmaier [79], the local dislocation density $\rho_d(r)$ was computed with a code programmed ad hoc by the authors. The tool defines hemispherical shells and by using the DXA output, classifies the dislocation contribution to each shell
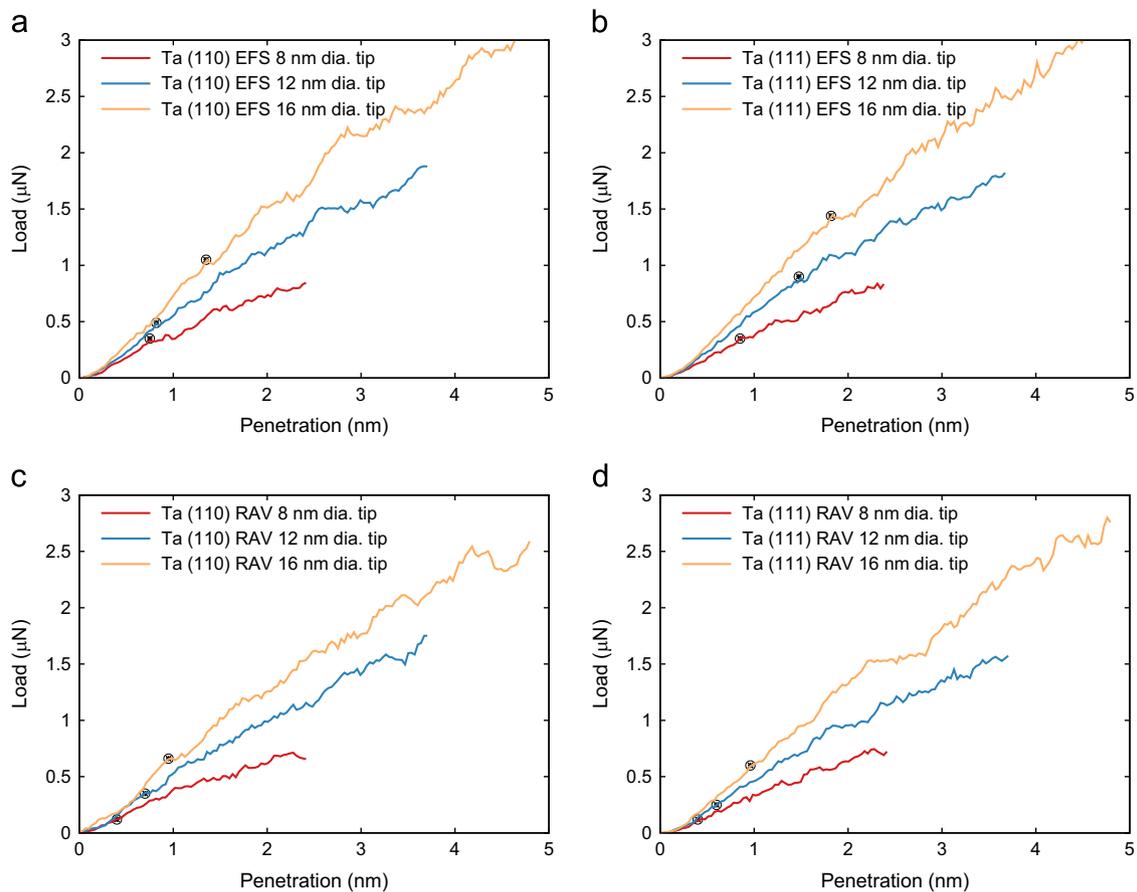
**Fig. 8.** Ta (110) and (111): indenter size dependence of the loading curves for 8, 12 and 16 nm diameter tip as described by (a and b) Dai-EFS and (c and d) Ravelo-EAM potentials. Markers indicate the onset of plasticity.
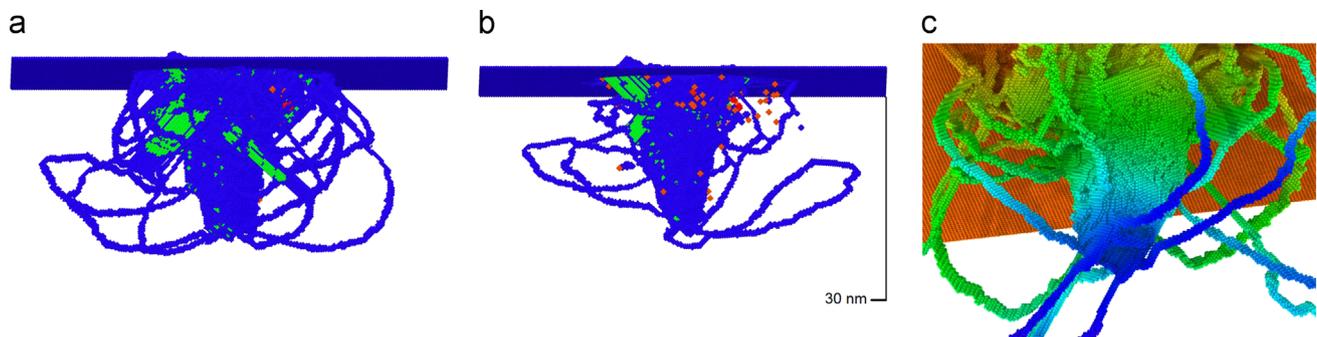


**Fig. 9.** (a) Twinning for the Li-EAM potential at the end of the loading stage, and (b) at the end of the recovery stage, with twin boundaries shown in green, point defects in red, and other defects in blue, as filtered by the Dislocation Extraction Algorithm. (c) Close-up of the residual defective structures for Li-EAM, showing a nest-like structure. Colors indicate distance from surface, with blue being deeper into the sample. Loading direction: [100]. (a) Li-EAM, end load twinning, (b) Li-EAM, residual twinning and (c) close up – nest-like structure. (For interpretation of the references to color in this figure caption, the reader is referred to the web version of this article.)

and finally computes the dislocation density associated to each shell. Shell thickness was taken as 1 nm. The dislocation density was computed as the total length divided by the volume of the shell. The results are presented in Fig. 11 showing the computed local dislocation density as a function of the distance to the center of the spherical indenter. There is no significant effect of orientation on the density, which decays from a maximum around $10^{17}$ m$^{-2}$ to less than $10^{16}$ m$^{-2}$ over a distance approximately equal to the indenter radius. This agrees with earlier works [35,36] and experimental measurements showing that the plastic deformation is around 2–3 times the radius $a_p$. The curves show distinctive features such as a maximum at a distance to the indented surface and decay both towards the surface and to the substrate interior. As expected after previous experimental results

by Chiu and Ngan [80], the dislocation density, $\rho_d$, is a function of the depth within the sample, that is the local dislocation density varies with depth. A plausible explanation can be derived from the known fact that defect nucleation occurs where shear stresses are maximum; for the stress field exerted by a spherical indenter this happens at a typical distance of 0.48 $a_p$ in an isotropic solid [81]. Naturally, one would expect also a decay towards the surface, as seen in the density profiles in Fig. 12. It should be noted that it is difficult to measure the dislocation density close to a free surface using existing simulation analysis techniques. The comparison of the Dai-EFS and Ravelo-EAM potentials predictions of dislocation densities, shown in Fig. 12, reveals a similar maximum value of $10^{17}$ m$^{-2}$, and a decay for $r > r_{indenter}$. A dislocation density of $\sim 10^{16}$ m$^{-2}$ would put the dislocation separation at $\sim 10$ nm for a
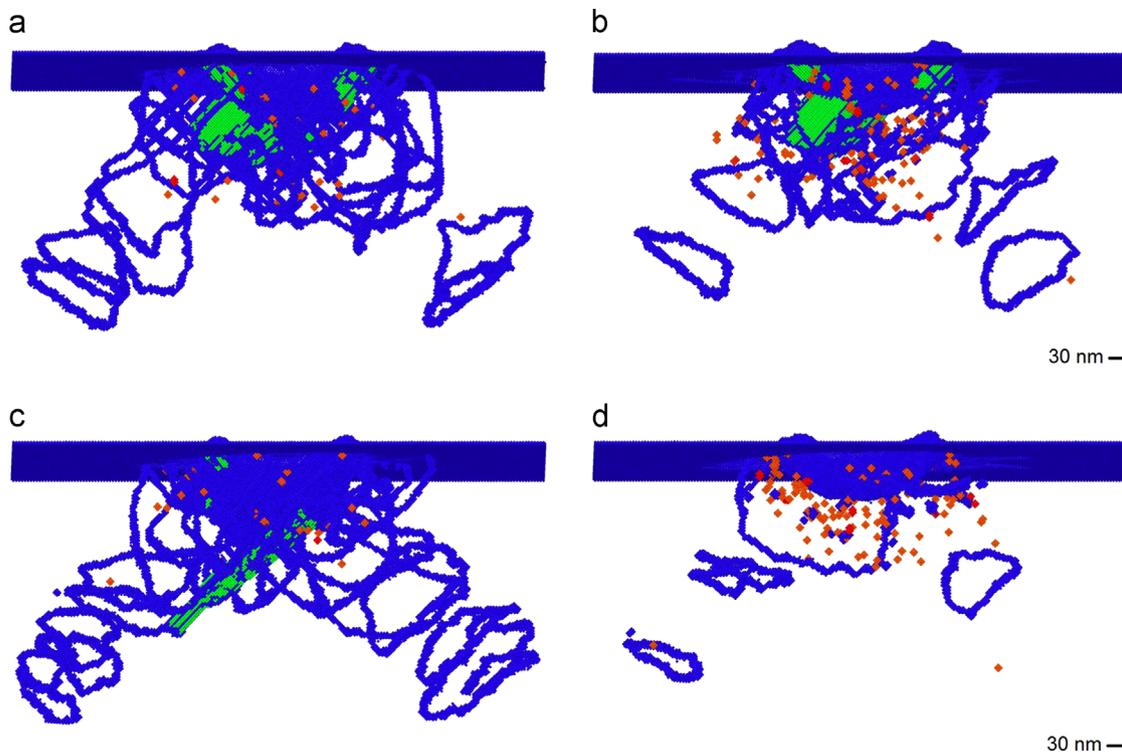
**Fig. 10.** Residual twinning for Dai-EFS and Ravelo-EAM potentials, with twin boundaries shown in green, point defects in red, and other defects in blue. Dislocation recovery is also verified during unloading. Loading direction: [100]. (a) Dai-EFS, end load twinning, (b) Dai-EFS, residual twinning, (c) Ravelo-EAM, end load twinning and (d) Ravelo-EAM, residual twinning. (For interpretation of the references to color in this figure caption, the reader is referred to the web version of this article.)
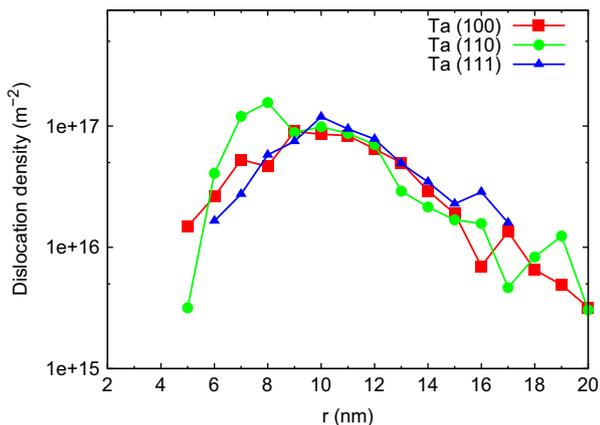


**Fig. 11.** Dislocation density profiles for the three orientations using a 16 nm diameter indenter on Dai-EFS potential Ta.

~10 nm indenter diameter, that is the mean spacing between dislocations would be of the same order as the indenter itself. Still, in the plastic zone created, a sufficiently large number of dislocations have been created (see Figs. 9 and 10) to give our distributions a meaningful sense.

### 4.6. Residual microstructures

Often left unexplored in previous MD studies of nanoindentation, we here study micro-structures after unloading. Bahr et al. [82] pointed out the possibility that a fraction of dislocations retreat to the surface during unloading. This is indeed verified in our simulations (Fig. 10) and was also shown recently by Smith and co-workers [43]. There is a significant recovery of defective structures for the Dai-EFS and Ravelo-EAM potentials. After the loading stage, the Ravelo-EAM potential has produced a significant amount of

prismatic loops on ⟨111⟩ directions. During the unloading stage several prismatic loops retreat towards the surface and interact with other dislocation loops, leading to their annihilation. This process also leads to the production of single and di-vacancies (Fig. 10). The same mechanism is observed for the Dai-EFS potential. Quantification of dislocation densities by means of the Dislocation Extraction Algorithm reveals a two fold decrease in dislocation density due to unloading. The residual dislocation densities in our simulations are similar to values measured experimentally for Ta samples deformed at high pressures [83].

For the Li-EAM potential a nest-like structure made of twins and other non-dislocation defects develops during the loading stage and, due to the stability of these structures, the nest survives to the unloading stage, as seen in Fig. 9. The intersecting structures made of twins are relatively stable after unloading, resulting in only a modest decrease of the twin volume fraction, from 0.8% to 0.6% (Fig. 9a and b), where twin volume fractions are calculated for the whole box volume. Dislocation loops remain attached to this nest-like structure.

For the Dai-EFS potential, a significant fraction of twins also survive after unloading: 0.2% versus 0.3% at the end of the loading stage. (Fig. 10b). Surprisingly, for the Ravelo-EAM potential, twins do not survive after unloading (Fig. 10d). Ongoing experiments using HRTEM on nanoindented single crystal Ta [84] will hopefully clarify which scenario is more relevant for realistic conditions.

### 4.7. Study of the residual pileups

During the analysis of nanoindentation experiments, pile-ups at the indenter site are often explored by Atomic Force Microscopy (AFM) [65]. After release, we extracted the pile-up pattern from our simulations for the 16 nm diameter tip, shown in Fig. 13.

Biener et al. [65] observed a 4-fold symmetry and anisotropy of the pile-up pattern when studying {100} Ta under a spherical indenter. This 4-fold symmetry is expected for indentation of a {100} surface in a cubic crystal, because of the 4-fold symmetry of
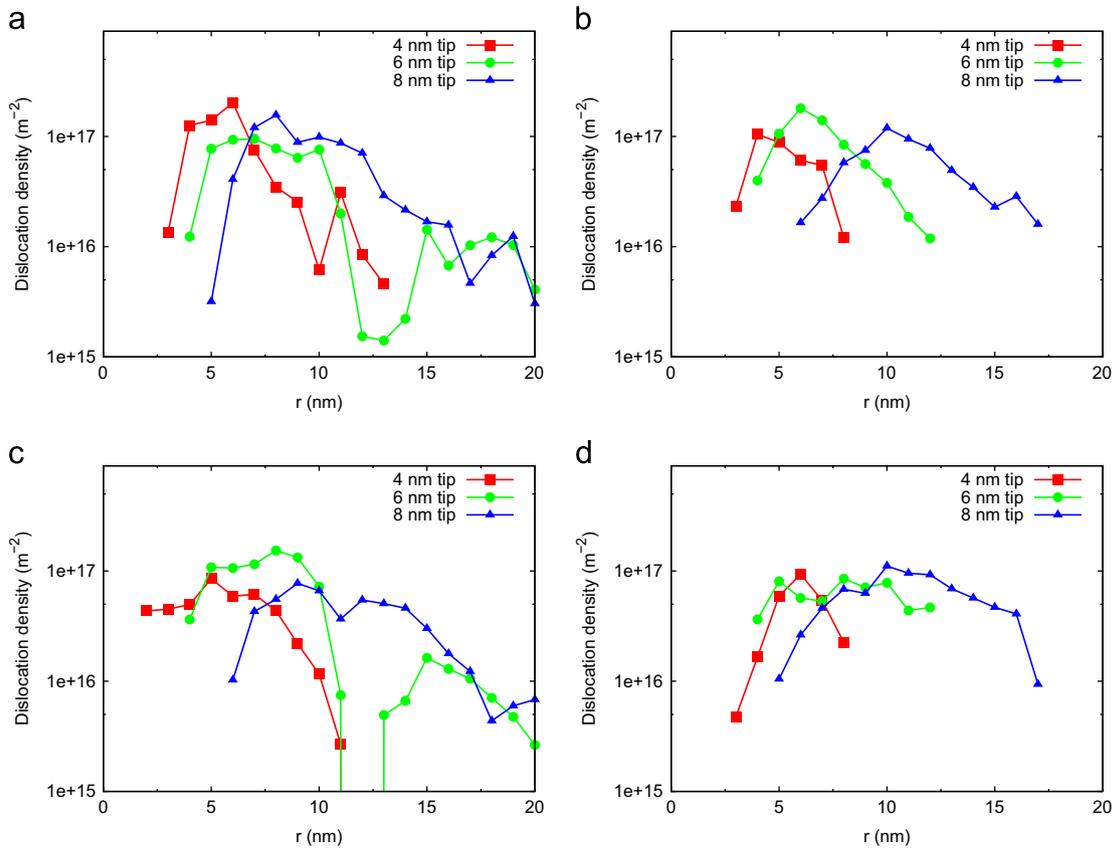
**Fig. 12.** Comparison of dislocation density profiles using Dai-EFS potential and Ravelo-EAM potential; (a and c) (110); (b and d) (111). (a) Dai-EFS, (b) Dai-EFS, (c) Ravelo-EAM and (d) Ravelo-EAM.
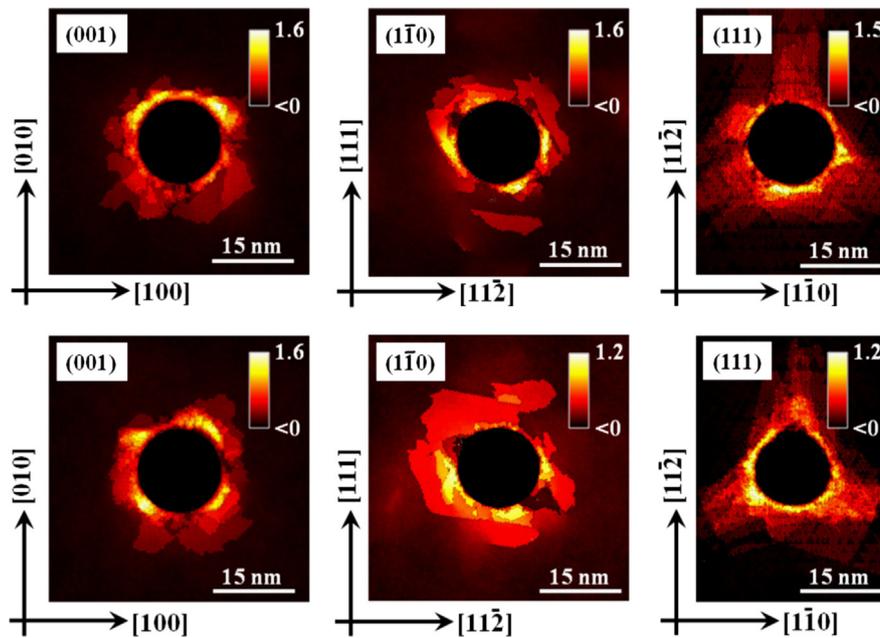


**Fig. 13.** Residual pile-ups. Results corresponding to the three crystallographic orientations for a 16 nm diameter indenter. Top row: Dai-EFS potential. Bottom row: Ravelo-EAM potential.

⟨111⟩ slip in this case. In a recent study of the plastic anisotropy of tungsten single cristals under spherical micro-indentation, Yao and co-workers [85] experimentally found the same pile-up anisotropy shown in Fig. 13. For the {110} surface, the ⟨111⟩ slip produces a 2-fold symmetry of the pile-up. Finally, for the {111} surface, the ⟨111⟩ slip produces a 3-fold symmetry of the pile-up

due to dislocation activity in $(11\overline{2})$, $(1\overline{2}1)$ and $(\overline{2}11)$ planes. In conclusion, Fig. 13 is in good agreement with experimental AFM images of Ta nanoindentation [65] and of W nanoindentation [85], in spite of the fact that length scales are much smaller here.

The height of the pile-ups is determined by net material transport towards the surface by loop emission and glide on

⟨111⟩ directions. Crystal plasticity models implemented in Finite Element Method (FEM) calculations are also able to predict pile-ups with the same geometry, but perfectly symmetric, i.e. equivalent in all planes [86,87]. Here thermal and stress fluctuations lead to slightly different hillocks on the surface. No significant differences are observed between the two potentials shown in Fig. 13, except for the fact that Dai-EFS potential seems to produce a less-spread out and steeper pile-up when compared to Ravelo-EAM potential.

### 4.8. Identification of an intrinsic length-scale from hardness simulations

The indentation size effect is the term usually used to refer to the increase in hardness with decreasing depth of penetration observed in many microindentation and nanoindentation studies [71]. This effect has been often treated using the concept of geometrically necessary dislocations associated with strain gradients. In order to identify the intrinsic material length parameter associated to GNDs, we will now follow the treatment by Al-Rub and Voyiadjis [61].

Considering the scheme presented in Fig. 4, we assume that the plastic deformation is accommodated by circular loops of geometrically necessary dislocations with Burgers vector normal to the plane of the sample surface. The determination of GNDs under a spherical indenter has been thoroughly treated [88,89,60,71]. The present treatment follows the approach of Al-Rub and Voyiadjis [61].

As the indenter is forced into the substrate of a single crystal, GNDs are required to accommodate the permanent shape change at the surface. It is common practice to assume that after spherical indentation, the profile of the residual pit in the unloaded condition can be described by a paraboloid defined as [90]

$$w_r = -h_p + r^2/D_p \quad \text{for } 0 \leq r \leq a_p \tag{19}$$

where $h_p$, $a_p$ and $D_p$ are the residual values of the profile depth, radius and diameter respectively, see Fig. 4. Here we propose a cubic fit of the indentation profile described by

$$w_r = -h_p + r^3/D_p^2 \quad \text{for } 0 \leq r \leq a_p \tag{20}$$

The cross-section of the pit is also of interest to both experimentalists and analysts in the nanoindentation field since material intrinsic length scales of strain gradient plasticity theory can be derived from it [61].

Fig. 14 presents the indentation residual profiles for the three crystallographic orientations under the EFS potential, together with the predictions of Eqs. (19) and (20), showing better agreement with the latter. This comparison becomes relevant for the analysis of plasticity in nanoindentation processes since, as shown by Al-Rub and Voyiadjis [61]; material intrinsic scales can be derived from the slope of Eq. (20). By taking the slope of Eq. (20) and comparing it with Fig. 4, it can be shown that

$$\left|\frac{dw}{dr}\right| = 3r^2/D_p^2 = \frac{b_G}{L_G} \quad \text{or} \quad L_G = \frac{b_G D_p^2}{3r^2} \tag{21}$$

where $L_G$ is the mean spacing between slip steps corresponding to the GND loops generated on the surface of the sample. The expression suggests that the spacing of dislocation loops increases as the observer moves away from the indentation axis (i.e. $L_G \propto 1/r^2$). This finding agrees with experimental observations [80]. Recently Faghihi and Voyiadjis [62] proposed two physically based models to capture the temperature and rate indentation size effects for bcc metals by considering different expressions of the geometrically necessary dislocations density. In that work, the authors present a physics-based equation for the material length scale of single-crystalline materials (see [62, Eq. 13]) which, for
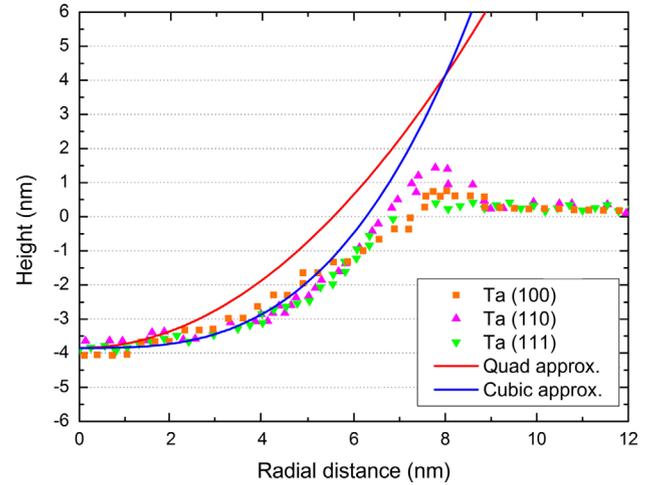


**Fig. 14.** Typical pit profiles for the current study compared to a quadratic approximation [90] and a cubic approximation by Eq. (25) for a 16 nm diameter indenter. Note the cross-over of Eq. (25) and the quadratic approximation which suggests that the former might only be applicable to shallow depths and or high indentation rates as the one used in the current study.

Niobium, renders a value of 2.94 nm, that is around 10 times the magnitude of the burgers vector. In our study, the use of Eq. (21) renders a value of ∼2 times the magnitude of the burgers vector. This difference is no surprise since Voyiadjis and Al-Rub [91] demonstrated that the length scale decreases with the increase of strain rate, which is a non-negligible condition of our MD simulations.

Continuing with our treatment, and defining $\lambda$ as the total length of the injected loops, then

$$d\lambda = 2\pi r \frac{dr}{L_G} = 6\pi \frac{r^3}{b_G D_p^2} dr \tag{22}$$

Integrating

$$\lambda = \int_0^{a_p} 6\pi \frac{r^3}{b_G D_p^2} dr = \frac{3}{2}\pi \frac{a_p^4}{b_G D_p^2} \tag{23}$$

The dislocation density during indentation is also governed by a large hemispherical volume $V$ defined by the contact radius $a_p$ around the indentation profile and a plasticity zone factor $f$, taken here as equal to 1.9 after Durst et al. [35]. This is consistent with the results of dislocation densities presented in Figs. 11 and 12. In this model, the injected loops remain within $V$; hence, assuming a half-sphere:

$$V = \frac{2}{3}\pi(fa_p)^3 \tag{24}$$

so that the density of GNDs becomes

$$\rho_G = \frac{\lambda}{V} = f^{-3} \frac{a_p}{b_G D_p^2} \tag{25}$$

Should Eq. (19) be used, instead of Eq. (20), $\rho_G$ will not be a function of the indentation depth, hence of the contact radius. This was demonstrated by Al-Rub and Voyiadjis [61], in agreement with Swadener et al. [71]. Therefore, Eq. (20) is worth an analysis. First of all, the results are a direct consequence of the profile of indentation pits which are $L_G \propto r^3$ instead of $r^2$, a change in profile evolution that may have been caused by the indentation rate that is much larger than in quasi-static indentation tests, or by the shallow penetration depth.

As shown by Gerberich et al. [92] in their interpretation of indentation size effects, the ratio of the contact area to the hemispherical volume of deforming material can be nearly constant for

shallow depths. Following the same line of thinking, if the ratio $q = a_p/D_p$ is nearly constant, this is indeed verified in our simulations, Eq. (20) turns into

$$\rho_G = f^{-3} q \frac{1}{b_G D_p} \qquad (26)$$

This result is in agreement with Swadener [71] since $\rho_G$ is independent of the indentation depth for spherical indenters.

Calculation of the geometrically necessary dislocation density by means of Eq. (25) using the data available in Fig. 14 with a Burgers vector of 0.286 nm for Ta and an $f$ factor of 1.9 after Durst et al. [35] renders a reasonable value of $\rho_G \approx 6 10^{16}$ m$^{-2}$, where $q$ was taken as $1/2$ for the sake of simplicity. We should note that the choice of $f$ at this nano-scale is not beyond questioning but a detailed study of the appropriate determination at this scale would require an extensive research effort in itself [93]. The higher dislocation densities observed in the MD simulations suggest that there is a significant number of statistically stored dislocations (SSD). The relative proportions of GND and SSD seem to vary with the radial distance.

## 5. Conclusions

We used molecular dynamics (MD) simulations to study plasticity during nanoindentation of a Ta (100), (110) and (111) single crystals and investigated the influence of the interatomic potential on the onset of plasticity and on the resulting microstructures, differentiating dislocation activity and twinning.

Our major findings are the following:

- Three interatomic potentials where thoroughly evaluated. The results presented here pose serious concerns on the applicability of the Li-EAM potential in high-pressure, high strain gradient applications such as nanoindentation simulations. The Dai-EFS potential proved to have the least sensitivity to variations of indenter tip diameter and indenting velocity when compared to a Hertz-like behavior. Dislocation activity proves to be the main plasticity mechanism, with twinning as a secondary mechanism.
- The geometrically necessary dislocation density obtained analytically, $\rho_G \approx 6 \times 10^{16}$ m$^{-2}$, compares favorably with DXA measurements from the MD simulations and suggests that the density of statistically stored dislocations is commensurate with that of GNDs
- A new intrinsic length-scale law is proposed. The model is derived from the indentation pit profile and making use of the geometrically necessary dislocations concept. An intrinsic length scale is obtained, feeding a dislocation length and dislocation density computation that produce results consistent with calculations performed using MD data, suggesting that the model might suit studies of shallow depth or high penetration rate nanoindentation.

The results presented here can help in the development of dislocation-based continuum theories [94], which become extremely important when considering surface and thin-substrate effects in nanoindentation studies. This study shows how different potentials can produce very different results. But despite all their possible limitations, molecular dynamics simulations can still offer important insights into plastic activity during indentation [95–97], guiding the interpretation of experiments with ever increasing resolution.

## References

[1] A.C. Fischer-Cripps, Nanoindentation, Mechanical Engineering Series, 2nd edition, Springer, New York, 2004.
[2] R. Armstrong, W. Elban, S. Walley, Int. J. Mod. Phys. B 27 (08) (2013).
[3] E. Weppelmann, M. Wittling, M.V. Swain, D. Munz, Indentation cracking of brittle thin films on brittle substrates, in: R.C. Bradt, D.P.H. Hasselman, D. Munz, M. Sakai, V.Y. Shevchenko (Eds.), Fracture Mechanics of Ceramics, Springer, Boston, MA, USA, 1996, pp. 475–486.
[4] A.A. Volinsky, J.B. Vella, W.W. Gerberich, Thin Solid Films 429 (1–2) (2003) 201–210.
[5] B. Yang, L. Riester, T. Nieh, Scr. Mater. 54 (7) (2006) 1277–1280.
[6] A. Bendavid, P. Martin, H. Takikawa, Thin Solid Films 360 (1–2) (2000) 241–249.
[7] P.M. Sargent, M.F. Ashby, Mater. Sci. Technol. 8 (7) (1992) 594–601.
[8] S. Veprek, J. Vac. Sci. Technol. A: Vac., Surf., Films 17 (5) (1999) 2401.
[9] W.C. Oliver, G.M. Pharr, J. Mater. Res. 7 (06) (1992) 1564–1583.
[10] C. Kelchner, S. Plimpton, J. Hamilton, Phys. Rev. B 58 (17) (1998) 11085–11088.
[11] A. Gouldstone, N. Chollacoop, M. Dao, J. Li, A. Minor, Y. Shen, Acta Mater. 55 (12) (2007) 4015–4039.
[12] K. Van Vliet, J. Li, T. Zhu, S. Yip, S. Suresh, Phys. Rev. B 67 (10) (2003).
[13] G. Ziegenhain, H.M. Urbassek, Philos. Mag. 89 (26) (2009) 2225–2238.
[14] J. Zimmerman, C. Kelchner, P. Klein, J. Hamilton, S. Foiles, Phys. Rev. Lett. 87 (16) (2001).
[15] T. Zhu, J. Mech. Phys. Solids 52 (3) (2004) 691–724.
[16] E. Lilleodden, J. Zimmerman, S. Foiles, W. Nix, J. Mech. Phys. Solids 51 (5) (2003) 901–920.
[17] G. Ziegenhain, H.M. Urbassek, A. Hartmaier, J. Appl. Phys. 107 (6) (2010) 061807.
[18] C. Begau, A. Hartmaier, E. George, G. Pharr, Acta Mater. 59 (3) (2011) 934–942.
[19] Y. Liang, Q. Wang, N. Yu, J. Chen, F. Zha, Y. Sun, Nanosci. Nanotechnol. Lett. 5 (5) (2013) 536–541.
[20] I. Salehinia, D. Bahr, Scr. Mater. 66 (6) (2012) 339–342.
[21] I. Salehinia, S. Lawrence, D. Bahr, Acta Mater. 61 (5) (2013) 1421–1431.
[22] I. Cheng, A.M. Hodge, et al., Scr. Mater. 69 (4) (2013) 295–298.
[23] N. Naveen Kumar, R. Tewari, P. Durgaprasad, B. Dutta, G. Dey, Comput. Mater. Sci. 77 (2013) 260–263.
[24] J. Alcalá, R. Dalmau, O. Franke, M. Biener, J. Biener, A. Hodge, Phys. Rev. Lett. 109 (7) (2012).
[25] J. Hagelaar, E. Bitzek, C. Flipse, P. Gumbsch, Phys. Rev. B 73 (4) (2006) 045425.
[26] A. Caro, J. Hetherly, A. Stukowski, M. Caro, E. Martinez, S. Srivilliputhur, L. Zepeda-Ruiz, M. Nastasi, J. Nucl. Mater. 418 (1) (2011) 261–268.
[27] Y. Li, D. Siegel, J. Adams, X.-Y. Liu, Phys. Rev. B 67 (12) (2003).
[28] J.A. Martinez, D.E. Yilmaz, T. Liang, S.B. Sinnott, S.R. Phillpot, Curr. Opin. Solid State Mater. Sci. 17 (6) (2013) 263–270.
[29] J.A. Moriarty, V. Vitek, V.V. Bulatov, S. Yip, J. Comput.-aided Mater. Des. 9 (2) (2002) 99–132.
[30] R. Ravelo, Q. An, T.C. Germann, B. Holian, Large-scale molecular dynamics simulations of shock induced plasticity in tantalum single crystals. Shock Compression Of Condensed Matter-2011: Proceedings of the Conference of the American Physical Society Topical Group on Shock Compression of Condensed Matter (vol. 1426, no. 1, pp. 1263–1266). AIP Publishing (2012).
[31] R. Ravelo, T. Germann, O. Guerrero, Q. An, B. Holian, Phys. Rev. B 88 (13) (2013) 134101.
[32] D. Tramontina, P. Erhart, T. Germann, J. Hawreliak, A. Higginbotham, N. Park, R. Ravelo, A. Stukowski, M. Suggit, Y. Tang, et al., High Energy Density Phys. 10 (2014) 9–15.
[33] S. Plimpton, J. Comput. Phys. 117 (1) (1995) 1–19.
[34] X.D. Dai, Y. Kong, J.H. Li, B.X. Liu, J. Phys.: Condens. Matter 18 (19) (2006) 4527–4542.
[35] K. Durst, B. Backes, M. Göken, Scr. Mater. 52 (11) (2005) 1093–1097.
[36] K. Durst, B. Backes, O. Franke, M. Göken, Acta Mater. 54 (9) (2006) 2547–2555.
[37] H. Tsuzuki, P.S. Branicio, J.P. Rino, Comput. Phys. Commun. 177 (6) (2007) 518–523.
[38] A. Stukowski, K. Albe, Model. Simul. Mater. Sci. Eng. 18 (8) (2010) 085001.

[39] A. Stukowski, V.V. Bulatov, A. Arsenlis, Model. Simul. Mater. Sci. Eng. 20 (8) (2012) 085007.
[40] A. Stukowski, J. Mater. (2013) 1–9.
[41] A. Stukowski, Model. Simul. Mater. Sci. Eng. 18 (1) (2010) 015012.
[42] M.S. Daw, M.I. Baskes, Phys. Rev. B 29 (12) (1984) 6443.
[43] L. Smith, J.A. Zimmerman, L.M. Hale, D. Farkas, Model. Simul. Mater. Sci. Eng. 22 (4) (2014) 045010.
[44] M.A. Meyers, K.K. Chawla, Mechanical Behavior of Materials, Cambridge University Press, Cambridge, New York, 2009.
[45] A. Reuss, ZAMM – Zeit Angew. Math. Mech. 9 (1) (1929) 49–58.
[46] W. Voigt, Lehrbuch der kristallphysik:(mit ausschluss der kristalloptik), vol. 34, BG Teubner, 1928.
[47] W. Stewart, J. Roberts, N. Alexandropolous, K. Salama, J. Appl. Phys. 48 (1) (1977) 75–81.
[48] G. Kimminau, P. Erhart, E.M. Bringa, B. Remington, J.S. Wark, Phys. Rev. B 81 (9) (2010) 092102.
[49] M. Duesbery, V. Vitek, Acta Mater. 46 (5) (1998) 1481–1492.
[50] Y. Tang, E.M. Bringa, B.A. Remington, M.A. Meyers, Acta Mater. 59 (4) (2011) 1354–1372.
[51] D. Segall, A. Strachan, W.A. Goddard III, S. Ismail-Beigi, T. Arias, Phys. Rev. B 68 (1) (2003) 014104.
[52] L. Yang, P. Söderlind, J.A. Moriarty, Philos. Mag. A 81 (5) (2001) 1355–1385.
[53] S. Traiviratana, E.M. Bringa, D.J. Benson, M.A. Meyers, Acta Mater. 56 (15) (2008) 3874–3886.
[54] G.S. Fanourgakis, V. Pontikis, G. Zérah, Phys. Rev. B 67 (9) (2003) 094102.
[55] A. Cao, J. Appl. Phys. 108 (11) (2010) 113531.
[56] H. Hertz, Ueber die berührung fester elastischer körper, J. Angew. Math. (Crelle's Journal) 92 (1882).
[57] J.J. Vlassak, W.D. Nix, Philos. Mag. A 67 (5) (1993) 1045–1056.
[58] J.J. Vlassak, W. Nix, J. Mech. Phys. Solids 42 (8) (1994) 1223–1245.
[59] M. Ashby, Philos. Mag. 21 (170) (1970) 399–424.
[60] W.D. Nix, H. Gao, J. Mech. Phys. Solids 46 (3) (1998) 411–425.
[61] R.K. Abu Al-Rub, G.Z. Voyiadjis, Int. J. Plast. 20 (6) (2004) 1139–1182.
[62] D. Faghihi, G.Z. Voyiadjis, Mech. Mater. 44 (2012) 189–211.
[63] A. Barnoush, Acta Mater. 60 (3) (2012) 1268–1277.
[64] D. Lorenz, A. Zeckzer, U. Hilpert, P. Grau, H. Johansen, H. Leipner, Phys. Rev. B 67 (17) (2003).
[65] M. Biener, J. Biener, A. Hodge, A. Hamza, Phys. Rev. B 76 (16) (2007).
[66] S. Ogata, Science 298 (5594) (2002) 807–811.
[67] K. Rajulapati, M. Biener, J. Biener, A. Hodge, Philos. Mag. Lett. 90 (1) (2010) 35–42.
[68] H.-S. Park, N. Barton, J.L. Belof, K.J.M. Blobaum, R.M. Cavallo, A.J. Comley, B. Maddox, M.J. May, S.M. Pollaine, S.T. Prisbrey, B. Remington, R.E. Rudd, D.W. Swift, R.J. Wallace, M.J. Wilson, A. Nikroo, E. Giraldez, Experimental results of tantalum material strength at high pressure and high strain rate. Shock Compression of Condensed Matter-2011: Proceedings of the Conference of the American Physical Society Topical Group on Shock Compression of Condensed Matter (vol. 1426, no. 1, pp. 1371–1374). AIP Publishing (2012).
[69] C.A. Schuh, J.K. Mason, A.C. Lund, Nat. Mater. 4 (8) (2005) 617–621.
[70] K. Kang, V.V. Bulatov, W. Cai, Proc. Natl. Acad. Sci. 109 (38) (2012) 15174–15178.
[71] J. Swadener, J. Mech. Phys. Solids 50 (4) (2002) 681–694.
[72] A. Rajendran, R. Garrett, J. Clark, T. Jungling, J. Mater. Shap. Technol. 9 (1) (1991) 7–20.
[73] K. Hoge, A. Mukherjee, J. Mater. Sci. 12 (8) (1977) 1666–1672.
[74] Y. Tang, E.M. Bringa, M.A. Meyers, Acta Mater. 60 (12) (2012) 4856–4865.
[75] A. Higginbotham, M. Suggit, E. Bringa, P. Erhart, J. Hawreliak, G. Mogni, N. Park, B. Remington, J. Wark, Phys. Rev. B 88 (10) (2013) 104105.
[76] Y.M. Wang, A.M. Hodge, J. Biener, A.V. Hamza, D.E. Barnes, K. Liu, T.G. Nieh, Appl. Phys. Lett. 86 (10) (2005) 101915.
[77] A. Arsenlis, D. Parks, Acta Mater. 47 (5) (1999) 1597–1611.
[78] H. Gao, Y. Huang, Scr. Mater. 48 (2) (2003) 113–118.
[79] J. Hua, A. Hartmaier, Model. Simul. Mater. Sci. Eng. 18 (4) (2010) 045007.
[80] Y. Chiu, A. Ngan, Acta Mater. 50 (10) (2002) 2677–2691.
[81] M.A. Meyers, K.K. Chawla, Mechanical Metallurgy: Principles and Applications, vol. 38, Prentice-Hall, Englewood Cliffs, NJ, 1984.
[82] D. Bahr, D. Kramer, W. Gerberich, Acta Mater. 46 (10) (1998) 3605–3617.
[83] C.-H. Lu, B. Remington, B. Maddox, B. Kad, H.-S. Park, S. Prisbrey, M. Meyers, Acta Mater. 60 (19) (2012) 6601–6620.
[84] T. Remington, B. Kad, S. Zhao, B. Remington, M.A. Meyers, in preparation.
[85] W. Yao, C. Krill III, B. Albinski, H.-C. Schneider, J. You, J. Mater. Sci. 49 (10) (2014) 3705–3715.
[86] O. Casals, J. Očenášek, J. Alcala, Acta Mater. 55 (1) (2007) 55–68.
[87] O. Casals, S. Forest, Comput. Mater. Sci. 45 (3) (2009) 774–782.
[88] M. De Guzman, G. Neubauer, P. Flinn, W. Nix, in: Materials Research Symposium Proceedings, 1993.
[89] N. Stelmashenko, M. Walls, L. Brown, Y.V. Milman, Acta Metall. Mater. 41 (10) (1993) 2855–2865.
[90] S. Kucharski, Z. Mroz, Mater. Sci. Eng. A 318 (1) (2001) 65–76.
[91] G.Z. Voyiadjis, R.K.A. Al-Rub, Int. J. Solids Struct. 42 (14) (2005) 3998–4029.
[92] W.W. Gerberich, N.I. Tymiak, J.C. Grunlan, M.F. Horstemeyer, M.I. Baskes, J. Appl. Mech. 69 (4) (2002) 433.
[93] Y. Gao, C.J. Ruestes, D.R. Tramontina, H.M. Urbassek, submitted for publication.
[94] K. Schulz, D. Dickel, S. Schmitt, S. Sandfeld, D. Weygand, P. Gumbsch, Model. Simul. Mater. Sci. Eng. 22 (2) (2014) 025008.
[95] M. Lodes, A. Hartmaier, M. Göken, K. Durst, Acta Mater. 59 (11) (2011) 4264–4273.
[96] G.J. Tucker, S.M. Foiles, Mater. Sci. Eng. A 571 (2013) 207–214.
[97] S. Goel, S.S. Joshi, G. Abdelal, A. Agrawal, Mater. Sci. Eng. A. 597 (2014) 331–341.